1250 *Inorg. Chem.* **2011**, *50*, 1250–1257
DOI: 10.1021/ic1016559

Inorganic Chemistry
Article

Atomic Interactions in the p-Type Clathrate I $Ba_8Au_{5.3}Ge_{40.7}$

Hui Zhang,[†,‡] Horst Borrmann,[†] Niels Oeschler,[†] Christophe Candolfi,[†] Walter Schnelle,[†] Marcus Schmidt,[†] Ulrich Burkhardt,[†] Michael Baitinger,[†] Jing-Tai Zhao,[‡] and Yuri Grin*[,†]

[†] *Max-Planck-Institut für Chemische Physik fester Stoffe, Nöthnitzer Strasse 40, 01187 Dresden, Germany, and* [‡] *Key Laboratory of Transparent Opto-Functional Inorganic Materials, Chinese Academy of Sciences* (*Shanghai Institute of Ceramics*), *1295 Dingxi Road, 200050 Shanghai, China*

Received August 14, 2010

Single crystals of $Ba_8Au_{5.3}Ge_{40.7}$ [space group $Pm\bar{3}n$ (No. 223), a = 10.79891(8) Å] were prepared by a Bridgman technique. The crystal structure refinement based on single-crystal X-ray diffraction data does not reveal any vacancies in the Au/Ge framework or in the cages. In addition to the ionic bonding between Ba and the anionic framework, a direct interaction between Ba and Au atoms was identified in $Ba_8Au_{5.3}Ge_{40.7}$ by applying the electron localizability indicator. As expected by the chemical-bonding picture, $Ba_8Au_{5.3}Ge_{40.7}$ is a diamagnet and shows p-type electrical conductivity with a hole carrier concentration of 7.14×10^{19} cm^{-3} at 300 K and very low lattice thermal conductivity of $\approx$0.6 W m^{-1} K^{-1} at 500 K. The thermoelectric figure of merit ZT of single crystals of $Ba_8Au_{5.3}Ge_{40.7}$ attains 0.3 at 511 K and reaches 0.9 at 680 K in a polycrystalline sample of closely similar composition. This opens up an opportunity for tuning of the thermoelectric properties of materials in the Ba−Au−Ge clathrate system by changing the chemical composition.

Introduction

Intermetallic clathrates are known for their large variety of compositions and properties ranging from metallic conductors to semiconductors.[1,2] A common feature of all of these phases is their low heat conductivity.[3−5] The electrical transport properties and the electronic thermal conductivity of clathrates are controlled mainly by the framework atoms and depend strongly on the chemical composition as well as the amount and distribution of defects in the framework. This opens up the possibility of optimizing the thermoelectric performance by tuning the composition and bonding interaction between guest and host atoms. The necessary control of the charge carrier concentration requires reproducibility in the preparation and high-level characterization.

Especially, Ba-containing clathrates are considered to be prospective thermoelectrics. Three clathrate phases—$Ba_8Ge_{43}\square_3$[6−12] (clathrate I, space group $Ia\bar{3}d$), $BaGe_5$[13] (new clathrate type, space group $Pmna$), and Ba_6Ge_{25}[14−16] (clathrate IX, space group $P4_132$)—exist in the binary system Ba−Ge. In addition to difficulties in the preparation, these binary phases are not directly suitable for thermoelectric applications because of their either too large or too low charge carrier concentration considering the electronic balances $[Ba^{2+}]_8[(3b)Ge^-]_{12}[(4b)Ge^0]_{31} \times 4e^-$, $[Ba^{2+}]_6[(3b)Ge^-]_8[(4b)Ge^0]_{17} \times 4e^-$, and $[Ba^{2+}]\ [(3b)Ge^-]_2[(4b)Ge^0]_3 \times 0e^-$. Introducing a third component without changing the crystal structure may be one way to solve the problem. Ternary substitution variants of the clathrate I phase $Ba_8Ge_{43}\square_3$ of composition $Ba_8(T,Ge)_6Ge_{40}$ with T = Ni, Pd, Pt, Cu, Ag, and Au have been structurally characterized

*To whom correspondence should be addressed. E-mail: grin@cpfs.mpg.de. Tel.: +49-351-46464000.

(1) Cros, C.; Pouchard, M. *C. R. Chim.* **2009**, *12*, 1014–1056.
(2) Kovnir, K. A.; Shevelkov, A. V. *Russ. Chem. Rev.* **2004**, *73*, 923–938.
(3) Nolas, G. S.; Cohn, J. L.; Slack, G. A.; Schujman, S. B. *Appl. Phys. Lett.* **1998**, *73*, 178–180.
(4) Koza, M.; Johnson, M. R.; Viennois, R.; Mutka, H.; Girard, L.; Ravot, D. *Nat. Mater.* **2008**, *7*, 805–810.
(5) Christensen, M.; Abrahamsen, A. B.; Christensen, N. B.; Juranyi, F.; Andersen, N. H.; Lefmann, K.; Andreasson, J.; Bahl, C. R. H.; Iversen, B. B. *Nat. Mater.* **2008**, *7*, 811–815.
(6) Herrmann, R. F. W.; Tanigaki, K.; Kawaguchi, T.; Kuroshima, S.; Zhou, O. *Phys. Rev. B* **1999**, *60*, 13245.
(7) Carrillo-Cabrera, W.; Curda, J.; Peters, K.; Paschen, S.; Baenitz, M.; Grin, Y.; von Schnering, H. G. *Z. Kristallogr.—New Cryst. Struct.* **2000**, *215*, 321–322.
(8) Carrillo-Cabrera, W.; Budnyk, S.; Prots, Y.; Grin, Yu. *Z. Anorg. Allg. Chem.* **2004**, *630*, 2267–2276.
(9) Okamoto, N. L.; Oh, M. W.; Nishii, T.; Tanaka, K.; Inui, H. *J. Appl. Phys.* **2006**, *99*, 033513.
(10) Okamoto, N. L.; Tanaka, K.; Inui, H. *Acta Mater.* **2006**, *54*, 173–178.
(11) Candolfi, C.; Aydemir, U.; Baitinger, M.; Oeschler, N.; Steglich, F.; Grin, Yu. *J. Electron. Mater.* **2010**, *39*, 2039–2042.
(12) Aydemir, U.; Candolfi, C.; Borrmann, H.; Baitinger, M.; Ormeci, A.; Carrillo-Cabrera, W.; Chubilleau, C.; Lenoir, B.; Dauscher, A.; Oeschler, N.; Steglich, F.; Grin, Yu. *Dalton Trans.* **2010**, *39*, 1078–1088.
(13) Aydemir, U.; Akselrud, L.; Carrillo-Cabrera, W.; Candolfi, C.; Oeschler, N.; Baitinger, M.; Steglich, F.; Grin, Yu. *J. Am. Chem. Soc.* **2010**, *132*, 10984–10985.
(14) Carrillo-Cabrera, W.; Curda, J.; von Schnering, H. G.; Paschen, S.; Grin, Yu. *Z. Kristallogr.* **2000**, *215*, 207–208.
(15) Fukuoka, H.; Iwai, K.; Yamanaka, S.; Abe, H.; Yoza, K.; Häming, L. J. *Solid State Chem.* **2000**, *151*, 117–121.
(16) Carrillo-Cabrera, W.; Borrmann, H.; Paschen, S.; Baenitz, M.; Steglich, F.; Grin, Yu. *J. Solid State Chem.* **2005**, *178*, 715–728.

 Published on Web 01/20/2011

already in the 1990's.[17] The crystal structure of Ba_8T_x-$Ge_{46-x-y}\square_y$ contains substituent atoms T together with Ge and defects $\square$ at the 6*c* site of the space group $Pm\bar{3}n$. Their distribution depends on the preparation route, temperature, and composition. Ordering of defects and substituent atoms leads to the formation of superstructures or to a reduction of symmetry.[12,18,19] Ternary substitution variants Ba_8Cu_x-$Ge_{46-x-y}\square_y$,[20−23] $Ba_8Ni_xGe_{46-x-y}\square_y$,[24−27] $Ba_8Pd_xGe_{46-x-y}$,[28] $Ba_8Pt_xGe_{46-x-y}$,[29] $Ba_8Zn_8Ge_{38}$,[30−33] $Ba_8Cd_8Ge_{38}$,[33] K_8Hg_3-Ge_{43},[34] and $Ba_8(T,Ge)_{46}$ (T = Mn, Fe, Co)[35−38] have been reported under aspects of phase equilibrium, crystal structures, and properties. Because of their chemical composition, the majority of type I clathrates with transition metals are usually n-type materials and their thermoelectric figure of merit ZT is relatively low compared with that of the benchmark compound $Ba_8Ga_{16}Ge_{30}$ ($ZT \approx 0.8$ at 1050 K).[39] Only the just recently discovered n-type clathrate $Ba_8Ni_{0.31}Zn_{0.52}$-$Ga_{13.06}Ge_{32.2}$ shows a high ZT of 1.2 at 1000 K.[40] In a few cases, both p- and n-type conductivity were found in the same chemical system, depending on the composition. For example, the clathrate I phase in the system Ba−Ni−Ge was reported to exist over a homogeneity range of $0 \le x \le 0.6$ in $Ba_8Ni_{6-x}Ge_{40+x}$. Depending on the Ni content, a metal-to-insulator transition was found and the clathrate phase showed either p- or n-type conduction.[25] However, single crystals grown from the melt have the composition Ba_8-$Ni_{3.5}Ge_{42.1}\square_{0.4}$, which is outside of the previously reported homogeneity range, and exhibit n-type conductivity.[27]

The clathrate phase in the system Ba−Au−Ge was first described with the composition $Ba_8Au_6Ge_{40}$.[17] The electrical transport properties of the materials with this composition were investigated, and a bad-metal behavior was found.[6] To provide a basis for investigations on the homogeneity range of the clathrate I phase $Ba_8Au_xGe_{46-x-y}\square_y$ and to interpret the properties of polycrystalline materials, we prepared a single crystal as a reference material. Here we report the crystal structure, chemical bonding, and thermoelectric properties of the p-type clathrate $Ba_8Au_{5.3}Ge_{40.7}$.

Experimental Section

Synthesis. Polycrystalline samples of the nominal composition $Ba_8Au_{5.33}Ge_{40.67}$ and a mass of ∼15 g were prepared in an argon-filled glovebox [$c(O_2)$ and $c(H_2O) \le 1$ ppm]. Crystalline Ba (Alfa Aesar, 99.9% metal basis), Au powder (Chempur, 99.999% metal basis), and Ge pieces (Chempur, 99.9999%) were used as starting materials without further purification. First, the precursor BaGe was prepared by induction melting of the stoichiometric mixture of elements. Second, the stoichiometric amounts of BaGe, Au, and Ge were put in glassy graphite crucibles (Sigradur G, HTW, round head, ∅ = 13 mm, l = 63 mm), heated in an induction furnace to the melt stage, and cooled within a few minutes to room temperature. No mass loss was observed after this treatment. The products showed gray metallic luster and were stable in air as well as dilute HCl.

The Bridgman technique was applied to grow a single crystal. A polycrystalline sample with nominal composition Ba_8-$Au_{5.33}Ge_{40.67}$ was filled in a glassy graphite crucible (tip head, ∅ = 10 mm, l = 105 mm), heated at a rate of 10 K min^{-1} to 1125 °C under an Ar atmosphere, kept for 12 h, and then slowly moved down from the hot part of the resistivity furnace (HTM Reetz GmbH) for 80 mm within 96 h. The crystallinity of the obtained material was examined by metallography and X-ray diffraction. For investigation of the influence of the microstructure on the thermoelectric performance, the single-crystalline sample was ground and compacted by spark plasma sintering (SPS; Dr. Sinter 5155, Syntex Ltd., Tokyo, Japan).

Powder X-ray Diffraction (PXRD). Thoroughly ground specimens were characterized by the Guinier technique (Huber image plate camera G670, Cu Kα_1 radiation, λ = 1.54056 Å, $3° < 2\theta < 100°$, step width 0.005° of 2θ) using LaB_6 with the lattice parameter a = 4.1569 Å as an internal standard. Unit cell dimensions were determined by means of a least-squares technique with the program package *WinCSD*.[41]

Crystal Structure Investigation. A fragment of the single crystal with a size of $0.030 \times 0.025 \times 0.020$ mm^3 was fixed on top of the glass capillaries with grease. Diffraction data were collected with a rotating anode diffraction system Rigaku Spider (Varimax optical system, Ag Kα radiation, λ = 0.56087 Å). Absorption correction was performed by a multiscan procedure. The crystal structure refinement was made by employing a full-matrix least-squares procedure within the program package *WinCSD*.[41] For crystal structure presentation, the program *Atoms 6.0* was used.[42]

Microstructure Analysis. For metallographic investigations, the single-crystal samples were cut along the growth axis and

(17) Cordier, G.; Woll, P. *J. Less Common Met.* **1991**, *169*, 291–302.
(18) Dubois, F.; Fässler, T. *J. Am. Chem. Soc.* **2005**, *127*, 3264–3265.
(19) Kaltzoglou, A.; Hoffmann, S. D. *Eur. J. Inorg. Chem.* **2007**, *26*, 4162–4167.
(20) Li, Y.; Chi, J.; Gou, W.; Khandekar, S.; Ross, J. H., Jr. *J. Phys.: Condens. Mater.* **2003**, *15*, 5535–5542.
(21) Johnsen, S.; Bentien, A.; Madsen, G. K. H.; Iversen, B. B.; Nygren, M. *Chem. Mater.* **2006**, *18*, 4633–4642.
(22) Melnychenko-Koblyuk, N.; Grytsiv, A.; Rogl, P.; Schmid, H.; Giester, G. *J. Solid State Chem.* **2009**, *182*, 1754–1760.
(23) Zhang, H.; Zhao, J. T.; Tang, M. B.; Man, Z. Y.; Chen, H. H.; Yang, X. X. *J. Alloys Compd.* **2009**, *476*, 1–4.
(24) Bentien, A.; Johnsen, S.; Iversen, B. B. *Phys. Rev. B* **2006**, *73*, 094301.
(25) Johnsen, S.; Bentien, A.; Madsen, G. K. H.; Nygren, M.; Iversen, B. B. *Phys. Rev. B* **2007**, *76*, 245126.
(26) Zhang, H.; Zhao, J. T.; Tang, M. B.; Man, Z. Y.; Chen, H. H.; Yang, X. X. *J. Phys. Chem. Solids* **2009**, *70*, 312–315.
(27) Nguyen, L. T. K.; Aydemir, U.; Baitinger, M.; Bauer, E.; Borrmann, H.; Burkhardt, U.; Custers, J.; Haghighirad, A.; Höfler, R.; Luther, K. D.; Ritter, F.; Assmus, W.; Grin, Yu.; Paschen, S. *Dalton Trans.* **2010**, *39*, 1071–1077.
(28) Melnychenko-Koblyuk, N.; Grytsiv, A.; Rogl, P.; Rotter, M.; Bauer, E.; Durand, G.; Kaldarar, H.; Lackner, R.; Michor, H.; Royanian, E.; Koza, M.; Giester, G. *Phys. Rev. B* **2007**, *76*, 144118.
(29) Melnychenko-Koblyuk, N.; Grytsiv, A.; Rogl, P.; Rotter, M.; Lackner, R.; Bauer, E.; Fornasari, L.; Marabelli, F.; Giester, G. *Phys. Rev. B* **2007**, *76*, 195124.
(30) Alleno, E.; Maillet, G.; Rouleau, O.; Leroy, E.; Godart, C.; Carrillo-Cabrera, W.; Simon, P.; Grin, Yu. *Chem. Mater.* **2009**, *21*, 1485–1493.
(31) Melnychenko-Koblyuk, N.; Grytsiv, A.; Fornasari, L.; Kaldarar, H.; Michor, H.; Rohrbacher, F.; Koza, M.; Royanian, E.; Bauer, E.; Rogl, P.; Rotter, M.; Schmid, H.; Marabelli, F.; Devishvili, A.; Doerr, M.; Giester, G. *J. Phys.: Condens. Matter* **2007**, *19*, 216223.
(32) Borshch, N. A.; Pereslavtseva, N. S.; Kurganskii, S. I. *Semiconductors* **2009**, *43*, 590–594.
(33) Kuhl, B.; Czybulka, A.; Schuster, H. U. *Z. Anorg. Allg. Chem.* **1995**, *621*, 1–6.
(34) Kaltzoglou, A.; Ponou, S.; Fässler, T. F. *Eur. J. Inorg. Chem.* **2008**, 4507–4510.
(35) Grytsiv, A.; Melnychenko-Koblyuk, N.; Nasir, N.; Rogl, P.; Saccone, A.; Schmid, H. *Int. J. Mater. Res.* **2009**, *100*, 189–202.
(36) Kawaguchi, T.; Tanigaki, K.; Yasukawa, M. *Appl. Phys. Lett.* **2000**, *77*, 3438–3440.
(37) Yang, C. K.; Zhao, J.; Lu, J. P. *Phys. Rev. B* **2004**, *70*, 073201.
(38) Li, Y.; Ross, J. H., Jr.; Larrea, J. A.; Baggio-Saitovitch, E. *Physica C* **2004**, *408−410*, 869–871.
(39) Kuznetsov, V. L.; Kuznetsova, L. A.; Kaliazin, A. E.; Rowe, D. M. *J. Appl. Phys.* **2000**, *87*, 7871–7875.
(40) Shi, X.; Yang, J.; Bai, S. Q.; Yang, J. H.; Wang, H.; Chi, M. F.; Salvador, J. R.; Zhang, W. Q.; Chen, L. D.; Wong-Ng, W. *Adv. Fun. Mater.* **2010**, *20*, 755–763.
(41) Akselrud, L. G.; Zavalii, P. Yu.; Grin, Yu.; Pecharsky, V. K.; Baumgartner, B.; Wölfel, E. *Mater. Sci. Forum* **1993**, *133−136*, 335.
(42) Dowty, E. *Atoms 6.0*; Shape Software: Kingsport, TN, 2002.

mounted in a conductive resin (PolyFast, Struers). Specimens of a 2×3 mm^2 area were prepared by conventional multistep grinding and polishing processes, with final polishing using 0.25 μm diamond powder. Light optical microscopy (Axioplan2, Zeiss) as well as scanning electron microscopy (Philips XL30 with a LaB_6 cathode, FEI) confirmed the homogeneity of the microstructure. The chemical composition has been determined by wavelength-dispersive X-ray spectroscopy (WDXS) on a Cameca SX100 electron microprobe with a tungsten cathode using the intensities of the X-ray lines Ba Lα (4.46 keV), Au Lα (9.71 keV), and Ge Kα (9.89 keV). X-ray detectors equipped with the monochromator crystals pentaerythritol ($d = 8.742$ nm) and lithium fluoride ($d = 4.027$ nm) have been used. Count rates of approximately 10, 5, and 2 kcps for Ge Kα, Ba Lα, and Au Lα, respectively, result from excitation by an electron beam of 30 kV and 8 nA. Averaging on 10 points and the $\phi(\rho z)$-matrix correction model were applied.[43] The compound Ba_6Ge_{25} (31.21 wt % Ba and 68.79 wt % Ge) and elemental Au have been used as references for microprobe analyses.

Thermal Analysis. Measurements were performed utilizing a Netzsch DSC 404 C instrument. Approximately 20 mg of the sample in a glassy carbon crucible (∅ 2.5 mm, $l = 5$ mm) was sealed in a Nb ampule (∅ = 5 mm, $l = 15$ mm). The samples were heated under an Ar atmosphere with a heating rate of 10 K min^{-1} to 800 °C and then with 0.5 K min^{-1} to 1000 °C and then cooled to 100 °C with a cooling rate of 10 K min^{-1}.

Calculation Procedures. Electronic structure calculation and bonding analysis were carried out for the ordered model with the composition $Ba_8Au_6Ge_{40}$, with the 6*c* site occupied completely by Au and Ba2 atoms at the ideal position (6*d*) at the center of the cage. The *TB-LMTO-ASA* program package was used.[44] The von Barth−Hedin exchange potential[45] was employed for local-density approximation (LDA) calculations. The radial scalar-relativistic Dirac equation was solved to obtain partial waves. Because calculation within the atomic-sphere approximation (ASA) includes corrections for neglect of the interstitial regions and partial waves of higher order,[46] the addition of empty spheres was not necessary. The following radii of the atomic spheres were applied for the calculations: r(Ba1) = 2.525 Å, r(Ba2) = 2.769 Å, r(Au) = 1.469 Å, r(Ge2) = 1.452 Å, and r(Ge3) = 1.445 Å. A basis set containing Ba(6*s*,5*d*,4*f*), Ge(4*s*,4*p*), and Au(6*s*,6*p*,5*d*) orbitals was employed for a self-consistent calculation, with Ba(6*p*), Ge(4*d*), and Au(4*f*) functions being downfolded. A spin-polarized calculation was performed. The electron localizability indicator (ELI; γ) was evaluated in the ELI-D representation according to refs 47−49, with an ELI-D module within the program package *TB-LMTO-ASA*.[44]

Physical Properties. The sample was cut into specimens of $6 \times 6 \times 1$ and $1 \times 1 \times 6$ mm^3 size for measurement of the physical properties. The magnetic susceptibility was measured by a SQUID magnetometer (MPMS, Quantum Design) between 1.8 and 400 K in magnetic fields $\mu_0 H$ of up to 7 T. The Hall effect was measured in the temperature range from 10 to 300 K, with a Physical Property Measurement System (Quantum Design) applying magnetic fields up to 7 T. The carrier concentration (p) was calculated from the Hall coefficient $R_H = \rho_{xy}/\mu_0 H$ (assuming a Hall factor r_H of 1.0 in a single-carrier scheme; ρ_{xy} is the transversal resistivity) as $p = 1/eR_H$ or $n = -1/eR_H$, where p and n are the concentrations of the charge carriers (holes or electrons) and e is the charge of the electron. The Hall mobility μ_H was calculated from the Hall coefficient and electrical resistivity as $\mu_H = R_H/\rho$.

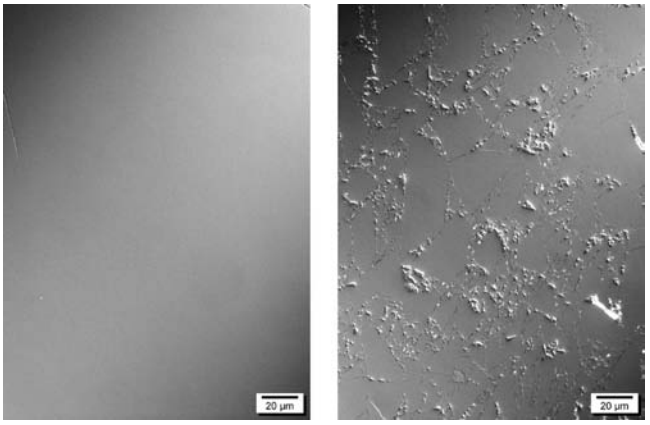

Figure 1. Light-field optical metallographic images for single crystal $Ba_8Au_{5.3}Ge_{40.7}$ (left) and the sample after SPS treatment (right).

The thermal diffusivity λ was determined in the temperature range from 300 to 750 K using the laser flash technique (LFA 447 Micro Flash, Netzsch). The thermal conductivity κ was derived from the relationship $\kappa \approx C_p d\lambda$, where d is the sample density and C_p the specific heat capacity. The latter was estimated according to Petit and Dulong with $C_p \approx 3NR/M$, where N is the number of atoms per formula unit, M the molar mass, and R the gas constant. No correction for thermal expansion was applied.

The electronic contribution κ_e to the thermal conductivity was calculated from the Wiedemann−Franz relationship $\kappa_e = L_0 T/\rho$, where ρ is the electrical resistivity and L_0 the Lorenz number according to the Drude−Sommerfeld theory, $L_0 = 2.44 \times 10^{-8}$ W Ω K^{-2}. The lattice thermal conductivity κ_L was obtained by subtracting the electronic thermal contribution from the total one. The electrical conductivity and Seebeck coefficient were measured simultaneously in the temperature range from 300 to 750 K using a ZEM-3 instrument (ULVAC-RIKO).

Results and Discussion

Composition and Crystal Structure. Gray polycrystalline specimens were obtained directly by induction melting of educts. A single-crystalline specimen of length of approximately 25 mm and diameter 10 mm was obtained using the Bridgman technique. The grain size and single-phase character of the sample was established from optical metallographic images (Figure 1). Metallographic analysis in combination with an X-ray diffraction investigation applying the Laue technique revealed the presence of single-crystalline domains of a size of approximately 3 mm in the sample. The composition $Ba_{7.94(5)}Au_{5.36(3)}Ge_{40.70(4)}$ was obtained by WDXS. The differential scanning calorimetry (DSC) experiment showed only one (endothermal) feature at 931(1) °C upon heating (Figure 2). In combination with the metallographic analysis results, this suggests a congruent melting of the clathrate I phase. The binary phase $Ba_8Ge_{43}\square_3$ forms peritectically.[8] The addition of gold leads to strong changes in the phase diagram of the ternary system Ba−Au−Ge in the vicinity of $Ba_8Ge_{43}\square_3$: the formation reaction of the clathrate phase changes from peritectic to congruent, and the formation temperature increases from 810 to 931 °C. In combination with the reduced symmetry of the crystal structure (see below), this points to the existence of two different clathrate I phases in the ternary system Ba−Au−Ge.

(43) Merlet, C. *Microchim. Acta* **1992**, *12*, 107.
(44) Jepsen, O.; Burkhardt, A.; Andersen, O. K. *The Program TB-LMTO-ASA*, version 4.7; Max-Planck-Institut für Festkörperforschung: Stuttgart, Germany, 1999.
(45) von Barth, U.; Hedin, L. *J. Phys. C* **1972**, *5*, 1629–1642.
(46) Andersen, O. K. *Phys. Rev. B* **1975**, *12*, 3060–3083.
(47) Kohout, M. *Int. J. Quantum Chem.* **2004**, *97*, 651–658.
(48) Kohout, M.; Wagner, F. R.; Grin, Yu. *Int. J. Quantum Chem.* **2006**, *106*, 1499–1507.
(49) Kohout, M. *Faraday Discuss.* **2007**, *135*, 43–54.

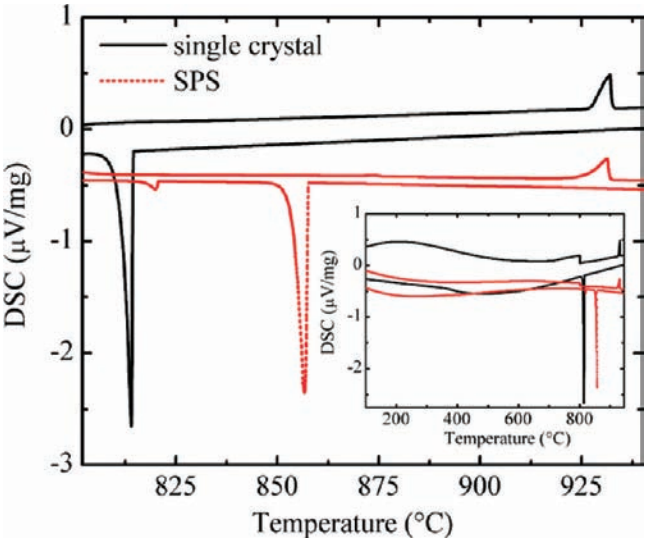

Figure 2. Thermal behavior (DSC measurement) of $Ba_8Au_{5.3}Ge_{40.7}$. Only one thermal effect is found in the temperature range between 800 and 1000 °C. The inset shows the whole temperature range measured; the step is caused by a change of the heating rate at 800 °C.

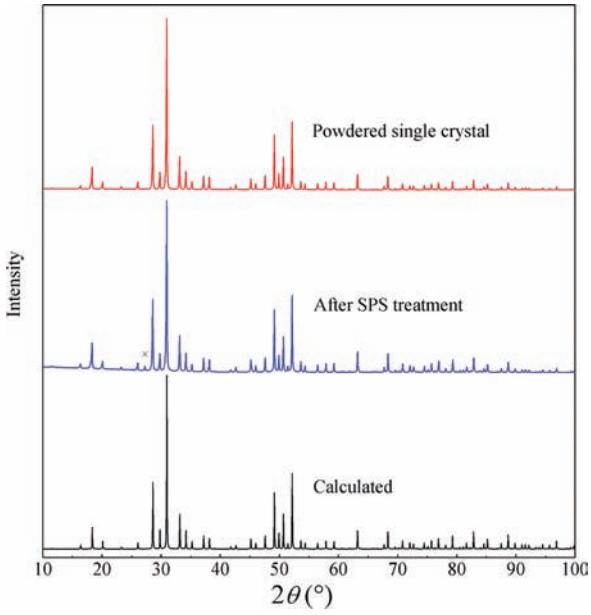

Figure 3. XRPD patterns of $Ba_8Au_{5.3}Ge_{40.7}$. A powdered single-crystalline sample (top) and an SPS-treated specimen produced from a powdered single crystal (bottom) are shown. The reflection positions of the clathrate I phase and elemental Ge (also marked by ×) are indicated by ticks.

From PXRD data, the lattice parameter of the single crystal was found to be $a = 10.79891(8)$ Å, which is close to the previously reported value of $a = 10.7987(1)$ Å for $Ba_8Au_6Ge_{40}$.[17] The PXRD pattern of a ground single crystal $Ba_8Au_{5.3}Ge_{40.7}$ is shown in Figure 3. The reflection intensities are in good agreement with the structure model derived from single-crystal diffraction data.

The refinement of the crystal structure was performed using single-crystal X-ray diffraction data. The high-resolution data set ($2\theta_{max} = 85.98°$ with Ag $K\alpha$ radiation, $\lambda = 0.56087$ Å) allowed the simultaneous refinement of the occupation and displacement parameters. In the first step of the structure refinement, the structure model of Cordier and Woll[17] with the overall composition $Ba_8Au_6Ge_{40}$ and all six Au atoms at the 6*c* site was applied. After refinement of the anisotropic displacement parameters, a fairly good value $R(F) = 0.037$ was obtained. The large B_{aniso} value of the Ba2 atoms was reduced by describing the electron density (ED) in this region by the split-position model (a quarter-occupied site 24*k* instead of a fully occupied 6*d* site), giving $R(F) = 0.033$, but remains still higher than that of Ba1.

The enlarged B_{iso} value by occupation of the 6*c* site with Au indicates the partial presence of defects or Ge atoms at this position only. An attempt to refine the crystal structure with defects and Au at this site led to a composition $Ba_8Au_{5.6}Ge_{40}$ deviating strongly from the results of chemical analysis. Thus, the scattering power of this site was described by the mixed occupation of Au and Ge [$Au_{0.883(2)}Ge_{0.117}$, $R(F) = 0.025$]. The final composition obtained from the crystal structure refinement is $Ba_8Au_{5.3(1)}Ge_{40.7(1)}$, which is in excellent agreement with chemical analysis of the single crystal presented above. Thus, the composition $Ba_8Au_{5.3}Ge_{40.7}$ is used for further discussions. Details concerning the data collection and structure refinement are given in Table 1. The final atomic parameters are listed in Table 2, and the interatomic distances and angles are shown in Table 3.

The clathrate I structure of $Ba_8Au_{5.3}Ge_{40.7}$ represents a space-filling combination of 20-atom dodecahedra at the corners and center of the cubic unit cell and 24-atom tetracaidecahedra forming three-dimensional rod packing along {100} (Figure 4). Ba1 resides at the 2*a* site in the center of the dodecahedron formed by Ge2 at the 16*i* site and Ge3 at the 24*k* site, respectively. In the description within the split-site model, Ba2 is located off-center in the tetracaidecahedra. In the Ge−Au framework, the angles in the planar six-rings of the 24-atom polyhedra constitute a less favorable bonding situation for the Ge atoms. The six-rings are condensed to infinite spirochains along the [100] direction via common atoms at site 6*c*.[12] Defects or substitution atoms in type I clathrates are, except for small atoms like boron in $K_7B_7Si_{39}$,[50] preferentially found at this position. All Ge atoms are 4-fold-bonded. The observed Ge−Ge distances of 2.50−2.55 Å are slightly larger than 2.45 Å observed in the elemental Ge with diamondlike crystal structure. In contrast, the distance Au−Ge of 2.51 Å is slightly shorter than the sum of the atomic (1.44 Å + 1.23 Å = 2.67 Å) or even covalent radii (1.34 Å + 1.22 Å = 2.56 Å) of the elements.[51] To understand this crystal chemical behavior of the framework, analysis of the chemical bonding was performed by applying the combined electron localizability/electron density (ELI-D/ED) approach.

Chemical Bonding. The features of the bonding picture were investigated by analysis of the ELI-D. In general, the ELI-D field divides the space into core basins surrounding the nuclei and the valence basins. This constitutes a principal difference of the ELI method compared to Bader's analysis of the ED,[52] where all basins are usually

(50) Jung, W.; Lörincz, J.; Ramlau, R.; Borrmann, H.; Prots, Y.; Haarmann, F.; Schnelle, W.; Burkhardt, U.; Baitinger, M.; Grin, Yu. *Angew. Chem., Int. Ed.* **2007**, *46*, 6725–6728.
(51) Emsley, J. *The Elements*, 3rd ed.; Oxford University Press: New York, 1998.
(52) Bader, R. F. W. *Atoms in Molecules, A Quantum Theory*; Clarendon Press and Oxford University Press Inc.: New York, 1994.

Table 1. Crystallographic Data for $Ba_8Au_{5.3}Ge_{40.7}$

composition	$Ba_8Au_{5.3}Ge_{40.7}$
molar mass/(g mol^{-1})	5098.99
crystal system	cubic
space group	$Pm\bar{3}n$ (No. 223)
lattice parameter a/Å	10.79891(8) (from PXRD data with LaB_6 as an internal standard)
unit cell volume /Å^3	1259.33(3)
formula unit per unit cell, Z	1
density ρ_{calc}/(g cm^{-3})	6.713(1)
diffraction system	Rigaku Spider
radiation; wavelength; monochromator	Ag $K\alpha$; $\lambda = 0.56087$ Å; multilayer optic
cryst size/mm^3	0.030 × 0.025 × 0.020
$2\theta_{max}$	85.98
μ/mm^{-1}	25.18
F(000)/e	2169
absorption correction	multiscan
no. of reflns collected; no. of reflns obsd [$I > 2\sigma(I)$]	10 521; 8610
no. of symmetry-independent reflns used in the refinement; R_{int}	1418; 0.047
refinement method	full-matrix least squares on F
refined parameters	21
residuals [$I > 2\sigma(I)$]	$R1(F) = 0.025$, $R1(F^2) = 0.033$, $wR_2 = 0.025$
extinction coefficient	0.000 377(4)

Table 2. Fractional Atomic Coordinates, Site Occupancies, and Isotropic (B_{iso}) and Anisotropic (B_{ij}) Atomic Displacement Parameters (Å^2) of $Ba_8Au_{5.3}Ge_{40.7}$

atom	site	x	y	z	occupancy	B_{iso}
Ba1	2a	0	0	0	1	0.706(2)
Ba2	24k	0.2432(6)	0.5140(5)	0	0.25	2.01(5)
Au1/	6c	$^1/_4$	0	$^1/_2$	0.883(2)/	0.845(2)
Ge1					0.117	
Ge2	16i	0.183 28(1)	x	x	1	0.660(2)
Ge3	24k	0	0.308 71(2)	0.117 92(2)	1	0.709(3)

atom	B_{11}	B_{22}	B_{33}	B_{12}	B_{13}	B_{23}
Ba1	0.706(4)	B_{11}	B_{11}	0	0	0
Ba2	1.44(9)	2.52(9)	2.06(6)	−0.13(5)	0	0
Au1/	1.212(5)	0.662(3)	B_{22}	0	0	0
Ge1						
Ge2	0.660(3)	B_{11}	B_{11}	−0.072(3)	B_{12}	B_{12}
Ge3	0.758(5)	0.671(5)	0.698(5)	0	0	−0.011(4)

Table 3. Selected Interatomic Distances (Å) and Angles (deg) in $Ba_8Au_{5.3}Ge_{40.7}$

Ba1−8Ge2	3.4281(2)	Ba2−2Ge3	3.740(5)
−12Ge3	3.5687(2)	−Ge3	4.037(5)
		−2Ge3	4.1668(9)
Ba2−2Ge2	3.876(4)	−Ge3	4.336(5)
−2Ge2	3.958(3)		
−2Ge2	4.107(3)	Au1−4Ge3	2.5103(2)
−2Ge2	4.135(4)		
−Au1	3.766(6)	Ge2−Ge2	2.4958(2)
−2Au1	3.770(4)	−3Ge3	2.5001(2)
−Au1	3.977(6)		
−2Ge3	3.491(5)	Ge3−Au1	2.5103(2)
−2Ge3	3.635(5)	−2Ge2	2.5001(2)
−2Ge3	3.666(6)	−Ge3	2.5468(3)
Ge3—Au1—Ge3	110.75(1)	Ge2—Ge3—Ge2	104.68(1)
Ge3—Au1—Ge3	108.83(1)	Ge2—Ge3—Ge3	106.40(1)
Ge2—Ge2—Ge3	107.89(1)	Ge2—Ge3—Au1	106.58(1)
Ge3—Ge2—Ge3	111.00(1)	Au1—Ge3—Ge3	124.62(1)

centered at the nuclei. While Bader's analysis of the ED gives the total amount and the charge difference between the different parts of the crystal structure, the combined ELI-D/ED analysis allows an understanding of how interactions between the different parts of the crystal structure are spatially organized.

The isosurface of ELI-D with $J = 1.24$ (Figure 5, top) reveals maxima (attractors) of the functional between the atoms within the Ge/Au framework. Each of the Ge−Ge contacts possesses its own ELI-D attractor, revealing

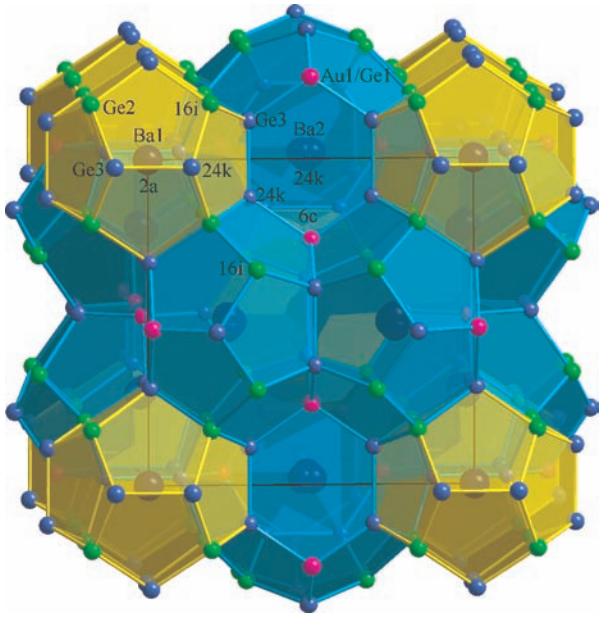

Figure 4. Crystal structure of $Ba_8Au_{5.3}Ge_{40.7}$: dark blue—Ba1 at the 2a site and Ba2 at the 24k site; pink—Au1/Ge1 at the 6c site; green—Ge2 at the 16i site; blue—Ge3 at the 24k site; yellow—dodecahedra; cyan—tetrakaidecahedra.

the direct (covalent) Ge−Ge interaction. If the local symmetry would be a cylindrical one—as in the isolated Ge_2 molecule[53]—the attractor would be located at the middle point of the Ge−Ge contact. In $Ba_8Au_6Ge_{40}$, the local symmetry is reduced and the attractors are shifted slightly off from the Ge−Ge axes. For the transition metal−Ge bonds, one would expect in the ELI-D representation ringlike attractors between the transition metal and Ge, as was found for a hypothetical isolated ScGe molecule.[53] In $Ba_8Au_6Ge_{40}$, the single-ring attractor is split into two parts (Figure 5, bottom). They together visualize the covalent character of the Au−Ge interaction.

The ELI-D in $Ba_8Au_6Ge_{40}$ shows spherelike regions of high ELI-D values around the atomic nuclei, revealing

(53) Kohout, M.; Wagner, F. R.; Grin, Yu. *Theor. Chem. Acc.* **2002**, *108*, 150–156.

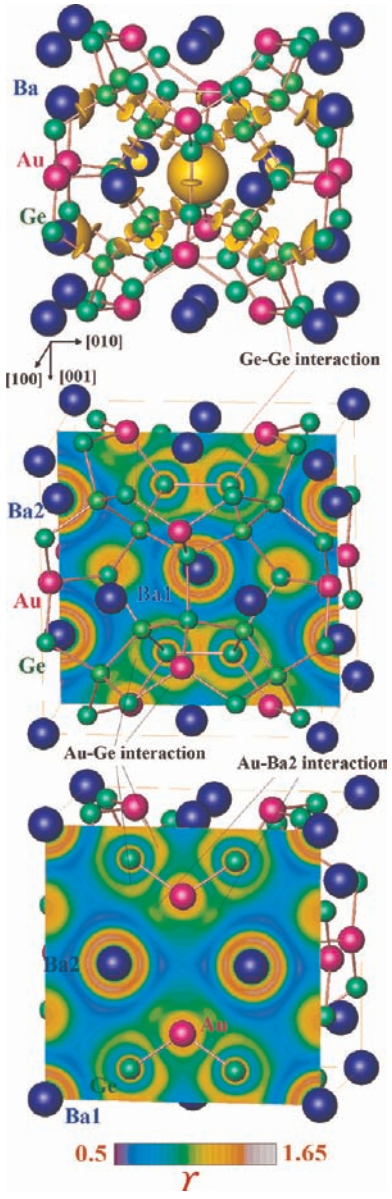

Figure 5. Electron localizability indicator J in $Ba_8Au_6Ge_{40}$: (top) ELI isosurface with $J = 1.24$ reveals Ge−Ge interaction; (middle) ELI map at $x = 0.5$ visualizing, in particular, the Ge−Ge bonding and Ba1−framework interaction; (bottom) ELI map at $x = 1$ emphasizing Au−Ge and Au−Ba2 interactions.

the atomic shell structure (the first five shells for Ba and Au and the first three shells for Ge; Figure 5, bottom). The penultimate ELI-D shells of Ba (fifth shell) are structured, more strongly for Ba2 than for Ba1 (Figure 5, middle, bottom); i.e., they deviate from the spherical symmetry characteristic for noninteracting isolated atoms. This can be quantified with the structuring index ε (the difference between the highest ELI-D value in the examined shell and the ELI-D value at which the localization domain does not have "holes").[54] The respective indexes for ELI-D are ε_Ba2 = 0.024 (fifth shell) and ε_Au = 0.027 (fifth shell), which are larger than the average ε_Ge = 0.011 for the third shell of Ge atoms and ε_Ba1 = 0.010 for the fifth shell of Ba1 atoms. Structuring of the inner ELI-D shells

(54) Wagner, F. R.; Bezugly, V.; Kohout, M.; Grin, Yu. *Chem.—Eur. J.* **2007**, *13*, 5724–5741.

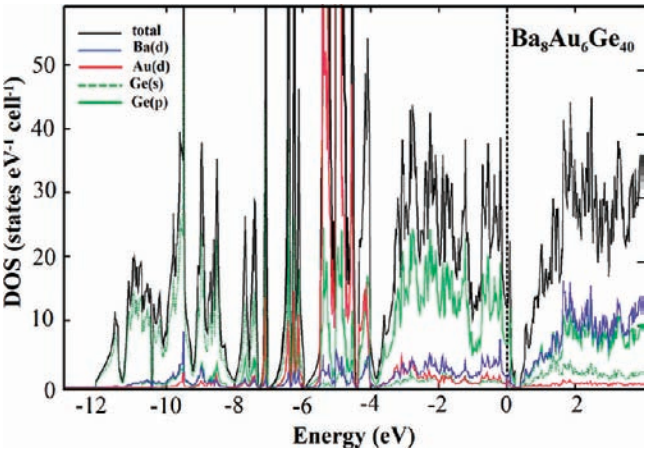

Figure 6. Total electronic density of states for $Ba_8Au_6Ge_{40}$ together with the partial contributions of selected atomic states. Assuming rigid-band behavior, the Fermi level for the $Ba_8Au_{5.3}Ge_{40.7}$ composition should be located in the band gap; for lower Au contents, it should be positioned at higher energies.

has been shown to be an indication for participation of the electrons of these shells in the bonding.[53,54] In addition to the structuring of the penultimate shells, a separate attractor is found between the Ba2 and Au atoms (Figure 5, bottom). In the isolated molecules ScGe[53] and TiF_4,[54] the appearance of a localizability maximum on the bond-opposite side of the transition-metal atom is mainly caused by the main-group ligand−transition metal covalent bonding. In the case of $Ba_8Au_6Ge_{40}$, this is in agreement with the covalent Au−Ge bonding described above. Contrary to the isolated molecules, the above-described maxima are located between the Ba2 and Au atoms, revealing also the Ba2−Au covalent interaction. For the intermetallic clathrates, an ionic interaction is often assumed between the host and guest atoms. In this case, a spherical distribution of ELI-D in the inner shells of the guest atom and the absence of dedicated attractors between the guest atoms and the framework should be expected. The attractors between Ba and Au atoms in $Ba_8Au_6Ge_{40}$ reveal the directed (covalent) interaction between the guest and framework in addition to the expected ionic one. In summary, the chemical bonding in $Ba_8Au_6Ge_{40}$ may be described by the formation of a three-dimenssional $[Au_6Ge_{40}]$ polyanion by Ge−Ge and Au−Ge bonds. Thus, Ba exhibits two types of interactions with the polyanion: one is more of an ionic nature with the charge transfer from Ba to the Ge−Ge and Au−Ge bonds in the polyanionic framework. The second interaction is a directed (covalent) one.

The electronic density of states (Figure 6) reveals that the s states of Ba contribute to a wide range of energies below the Fermi level and overlap with the *s* and *p* states of Ge as well as the *s* and *d* states of Au. This is in agreement with the picture of an ionic guest−host interaction in intermetallic clathrates. A special feature is the overlap of the *d* states of Au and Ba below the Fermi level between −7.5 and −6 eV as well as between −4 and 0 eV. If the region between −6 and −4 eV may be considered as nonbonding *d* states, then the two other regions mentioned above may be interpreted as bonding and antibonding parts for a Ba−Au interaction, which is in agreement with the bonding picture obtained from the ELI-D analysis. For $x = 6.0$, the density of states at the

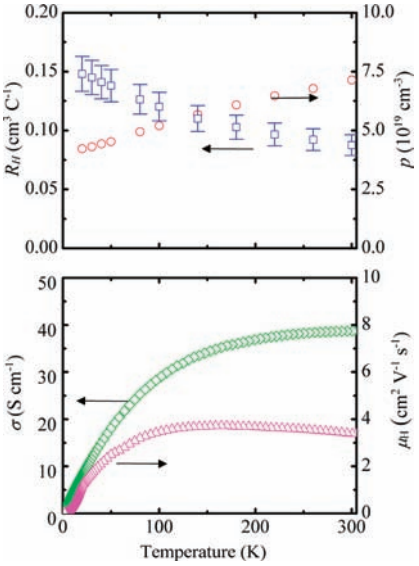

Figure 7. Temperature dependence of the Hall coefficient R_H, hole charge carrier concentration p, electrical conductivity σ, and carrier mobility μ_H for single-crystalline $Ba_8Au_{5.3}Ge_{40.7}$ in the temperature range from 10 to 300 K. The systematic inaccuracy originating from the shape of the specimen is ~10%.

Fermi level is about 10 states per electrovolt cell, while for $x < 5.33$, a hole-type semiconductor should be obtained.

Electronic, Thermal Transport, and Magnetic Properties. In agreement with the band-structure calculations, which did not reveal any localized magnetic moments, the magnetic susceptibility $\chi(T)$ of single-crystalline $Ba_8Au_{5.3}Ge_{40.7}$ is diamagnetic within the whole investigated temperature range and largely independent of the applied field. It exhibits a weak Curie-law-like upturn toward low temperatures, indicating the presence of minor Curie-paramagnetic impurities and/or magnetic point defects. An estimate of the maximum possible concentration of about 1.5×10^{-3} for such species can be made, assuming the smallest possible spin moment ($S = {}^1/_2$) for them. The intrinsic diamagnetic susceptibility is temperature-dependent and decreases with temperature. At 300 K, it is around -1.45×10^{-3} emu mol^{-1}.

According to the calculated electronic density of states for $Ba_8Au_xGe_{40}$ ($x = 6$; Figure 6), the Fermi level for $x = 5.33$ in a rigid-band approximation would be located at the top of the valence band. This is also in agreement with the Zintl-like electron count $[Ba^{2+}]_8[(4b)Au^{3-}]_{5.33}[(4b)Ge^0]_{40.67}$. For $x < 5.33$, antibonding states are occupied and the n-type conductivity should appear, while for $x > 5.33$, p-type conductivity should be present. Well in agreement with the calculation, single-crystalline $Ba_8Au_{5.3}Ge_{40.7}$ has a positive Hall coefficient R_H (Figure 7). The charge carrier concentration in a simple one-band model calculated from $p = 1/eR_H$ is 7.14×10^{19} cm^{-3} at 300 K, which corresponds to a value of 0.09 holes per unit cell: $[Ba^{2+}]_8[(4b)Au^{3-}]_{5.36}[(4b)Ge^0]_{40.64} \times 0.09p^+$.

The temperature dependencies of the electrical resistivity ρ, Seebeck coefficient α, thermal conductivity κ, and thermoelectric figure of merit $ZT = \alpha^2 T/\rho\kappa$ for single-crystalline $Ba_8Au_{5.3}Ge_{40.7}$ are shown in Figure 8. The electrical resistivity of the single crystal decreases with increasing temperature, showing a semiconductor-like

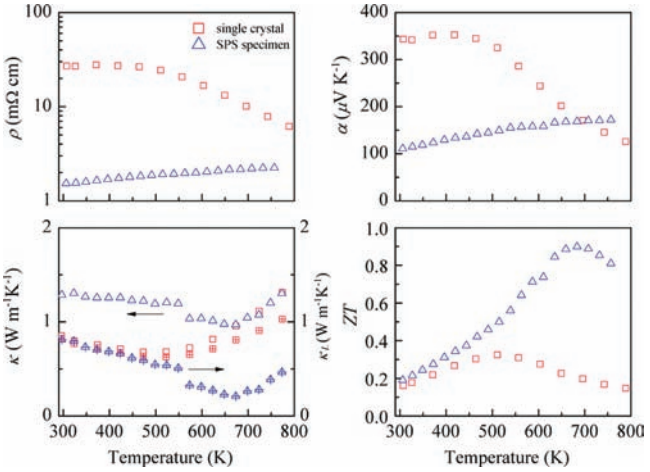

Figure 8. Temperature dependence of the electrical resistivity ρ, Seebeck coefficient α, total thermal conductivity κ (empty symbols) with lattice contribution κ_L (half-filled symbols), and the dimensionless thermoelectric figure of merit ZT for single-crystalline $Ba_8Au_{5.3}Ge_{40.7}$ (□) and SPS-treated specimen produced from a powdered single crystal (Δ).

behavior [$d\rho/dT < 0$, $\rho(300\ K) = 27$ mΩ m]. In the whole temperature range, the Seebeck coefficient α displays positive values, suggesting that holes dominate the electrical conduction, in agreement with the sign of R_H above. The Seebeck coefficient increases with increasing temperature to a maximum value of 370 μV K^{-1} at 450 K, resembling a close-to-semiconductor behavior. At high temperatures, the thermal excitation of minority carriers across the band gap is most likely the origin for the decrease of thermopower with temperature.

The width of the band gap E_g can be estimated as $E_g = 2e\alpha_{max}T(\alpha_{max})$ from the maximum value of the thermopower, α_{max}, and the temperature $T(\alpha_{max})$ at which this maximum occurs. With $T(\alpha_{max}) = 450$ K and $\alpha_{max} = 370$ μV K^{-1}, we obtain a band-gap width of 0.3 eV, while 0.1 eV is obtained from the band structure calculations for the $Ba_8Au_6Ge_{40}$ composition.

The total thermal conductivity κ is on the order of 1 W m^{-1} K^{-1} and is rather temperature-independent in the range from 300 to 750 K. The lattice thermal conductivity κ_L is obtained by subtracting the electronic contribution κ_e from the total thermal conductivity. Above room temperature, the lattice thermal conductivity reduces to approximately 0.6 W m^{-1} K^{-1} near 500 K. The coincidence of the temperature where the minimum of the thermal conductivity occurs with the temperature where the thermopower begins to decrease further corroborates the influence of minority carriers. Thus, this effect leads to an additional contribution, resulting in higher thermal conductivity values. The reasons for the low total thermal conductivity might be the mass difference between Ge and Au as well as the strain effect on the framework atoms in the 6*c* site. The additional Ba−Au interactions, especially for Ba2 positions, may be the key reason for this behavior. The combination of the electrical resistivity, thermopower, and thermal conductivity values leads to a value $ZT = 0.3$ at 511 K.

To investigate the influence of the microstructure on the thermal and electric transport behavior, a specimen was prepared from the finely ground single-crystalline $Ba_8Au_{5.3}Ge_{40.7}$ by SPS. Unexpectedly, the lattice parameter

of the clathrate I phase after SPS treatment changes significantly to 10.7973(1) Å and traces of elemental Ge were formed (Figures 1, 3). The lattice parameters of clathrates are very sensitive indicators for the charge carrier concentration, as was shown, e.g., for $Eu_8Ga_{16-x}Ge_{30+x}$.[55,56] Indeed, as suggested by the change of the lattice parameter, the transport properties of the SPS-treated sample changed strongly (Figure 8): the electrical conductivity increased by 1 order of magnitude, while the Seebeck coefficient increased toward higher temperatures. The figure of merit rises to $ZT = 0.9$ at 680 K, which is similar to $ZT = 0.8$ at 1050 K for $Ba_8Ga_{16}Ge_{30}$.[39] This observation opens up the opportunity for further optimization of the thermoelectric properties.

Conclusions

A millimeter-sized single-crystalline specimen of the type I clathrate $Ba_8Au_{5.3}Ge_{40.7}$ was grown using the Bridgman method. The crystal structure is characterized by the common occupation of the 6*c* site by Au and Ge, the off-center position of Ba2 in its cage in the framework, and Ba−Au covalent bonding interaction. The material is diamagnetic and is close to the Zintl-like valence-balanced composition, with slightly less than 184 electrons per unit cell assuming two-center two-electron bonds in the anionic framework. The single crystal exhibits p-type electrical conductivity with low thermal conductivity and a high Seebeck coefficient. The maximum of the thermoelectric figure of merit of the single crystal was found to be $ZT = 0.3$. The SPS-compacted finely ground sample with a slightly different composition shows a considerable increase of ZT up to 0.9 at 680 K, opening up the opportunity for further optimization of the thermoelectric properties.

Acknowledgment. Dr. G. Auffermann, Dr. M. Deppe, M. Eckert, R. Hempel-Weber, Dr. S. Hoffmann, S. Hückmann, R. Koban, S. Kostmann, P. Marasas, Dr. Y. Prots, Dr. I. Veremchuk, and P. Scheppan are acknowledged for discussions and assistance in the experiments. Financial support by the Partner Group Program between SIC CAS and MPI CPfS, National Basic Research Program of China (Grant 2007CB607503), and Natural Science Foundation of China (Grants 50821004, 5096-2004, and 21061004) is gratefully acknowledged.

(55) Pacheco, V.; Bentien, A.; Carrillo-Cabrera, W.; Paschen, S.; Steglich, F.; Grin, Yu. *Phys. Rev. B* **2005**, *71*, 165205.
(56) Bentien, A.; Pacheco, V.; Paschen, S.; Grin, Yu.; Steglich, F. *Phys. Rev. B* **2005**, *71*, 165206.